Intrinsic polarity inversion in III-nitride waveguides for efficient nonlinear interactions

M. Gromovyi,[1,4] N. Bhat,[2] H. Tronche,[3] P. Baldi,[3] M. El Kurdi,[1] X. Checoury,[1] B. Damilano,[2] ⓘ **and P. Boucaud[2,5]** ⓘ

[1]*Université Paris-Saclay, CNRS, C2N, 10 Boulevard Thomas Gobert, 91120 Palaiseau, France*
[2]*Université Côte d'Azur, CNRS, CRHEA, Rue Bernard Grégory, 06905 Sophia-Antipolis, France*
[3]*Université Côte d'Azur, CNRS, INPHYNI, 17 Rue Lauprêtre, 06200 Nice, France*
[4]*maksym.gromovyi@universite-paris-saclay.fr*
[5]*philippe.boucaud@crhea.cnrs.fr*

Abstract: III-nitrides provide a versatile platform for nonlinear photonics. In this work, we explore a new promising configuration – composite waveguides containing GaN and AlN layers with inverted polarity, i.e., having opposite signs of the $\chi^{(2)}$ nonlinear coefficient. This configuration allows us to address the limiting problem of the mode overlap for nonlinear interactions. Our modelling predicts a significant improvement in the conversion efficiency. We confirm our theoretical prediction with the experimental demonstration of second harmonic generation with an efficiency of $4\%\mathrm{W}^{-1}\mathrm{cm}^{-2}$ using a simple ridge waveguide. This efficiency is an order of magnitude higher compared to the previously reported results for III-nitride waveguides. Further improvement, reaching a theoretical efficiency of $30\%\mathrm{W}^{-1}\mathrm{cm}^{-2}$, can be achieved by reducing propagation losses.

1. Introduction

III-nitride semiconductors provide a promising platform for nonlinear photonics both for classical [1] and quantum applications [2]. Their non-centrosymmetric crystal structure can give rise to a second order nonlinearity. At the same time, their wide band gap offers a broad transparency window that spans from the ultra-violet to the mid-infrared range. This feature minimizes the issue of two-photon absorption in the telecom wavelength range, which is a main limiting factor for the conversion efficiencies at the high powers required for the nonlinear interactions [3]. Recently, there has been significant progress in the reduction of the propagation losses of the III-nitride waveguides. Ring resonators with quality factors reaching up to 2 million, and waveguides with less than 0.6 dB/cm propagation losses, have been reported. These achievements have enabled the demonstration of different nonlinear processes, such as second harmonic generation [4–7], optical parametric oscillation [8] and frequency combs generation [9,10].

Modal phase matching has been the primary approach used so far for the nonlinear interactions in III-nitride waveguides. In the case of second order processes, it requires an interaction between the fundamental modes in the infrared and the higher order modes in the visible. The conversion efficiency is directly proportional to the overlap of the interacting modes. This overlap integral can be as well included in an effective cross-section for the nonlinear process. In the case of a good overlap between two fundamental modes, this effective cross-section is close to the value of the geometric cross-section of the waveguide, namely the width multiplied by the height. However, for cases commonly used in nonlinear interactions, we deal with the overlap between the fundamental and the higher order modes which are orthogonal to each other at a given wavelength. Given that the modes are taken at different wavelengths, the overlap integral is not zero. However, it often remains very small, resulting in a large effective cross-section of the waveguides. As a consequence, the internal power densities are low, which is detrimental to

the efficiency of the nonlinear interactions. Therefore, maximizing the overlap integral of the interacting modes is of tremendous importance for achieving efficient nonlinear interactions.

Several approaches are known to address the issue of the harmonic conversion efficiency. The most common solution is based on the periodic modulation of the $\chi^{(2)}$ nonlinear coefficient along the direction of propagation in the waveguide, enabling a phase-matched interaction between fundamental modes. Such periodic modulation can be realized in ferroelectric materials such as LiNbO$_3$ [11,12], LiTaO$_3$ [13,14], and KTiOPO$_4$ [15,16] by inverting the crystal domains and, therefore, changing the sign of the $\chi^{(2)}$ coefficient through the application of a periodic electric field. However, achieving periodic domain inversion in III-nitrides remains a significant challenge. Several studies have been conducted using the approach of selective patterning and regrowth of GaN [17,18] and AlN [19,20]. The main challenge in this case is associated with the high propagation losses due to the macroscopically rough surface resulting from different growth rates domains with opposite polarity.

Another technique that allows an efficient nonlinear interaction between fundamental modes is based on the multi-layers waveguides which includes materials with a significant difference in the refractive indices. In this case, important dispersion differences can be obtained for the TM00 and TE00 modes due to the field discontinuities, enabling phase matching between fundamental modes of opposite polarization. A successful realization of such an approach was demonstrated in GaAs/AlOx waveguides [21–23]. However, this approach is not feasible for the III-nitride waveguides, as the refractive index contrast between GaN and AlN is not high enough in order to achieve the required dispersion difference for phase matching. Additionally, it should be noted that coupling between TM and TE modes is facilitated by the non-diagonal components $\chi^{(2)}_{zxx}$ and $\chi^{(2)}_{zxz}$ of the nonlinear tensor. For many materials, including III-nitrides, these components are smaller than the diagonal component like $\chi^{(2)}_{zzz}$. As a result, these interactions lead to lower conversion efficiencies.

There is also an approach based on the planar polarity inversion, which allows an interaction between the fundamental and higher order modes while preserving high values of the overlap integral. The overlap integral depends not only on the mode profiles but also on the nonlinear $\chi^{(2)}$ coefficient, as shown in Eq. (1). Therefore, one can significantly improve the value of the overlap by choosing a proper profile of the nonlinear coefficient distribution. The simplest solution that has been produced so far is based on the interaction between the TM00 pump and the TM10 harmonic with the inversion of the $\chi^{(2)}$ sign occuring right at the zero of the TM10 mode. This inversion can be achieved either directly during the growth [24] or through wafer bonding [25]. In III-nitrides, the TM modes are coupled through the largest component of the nonlinear tensor $\chi^{(2)}_{zzz}$. Therefore, in theory, this interaction may provide the highest possible conversion efficiency. So far, the realization of these approaches has been hindered by high propagation losses. The polarity inversion during the growth is associated with the high level of Mg doping required for the inversion and rough N-polar surface, both of which have a detrimental impact on the propagation losses. The wafer bonding approach faces similar problems due to the necessity of introducing a bonding layer in the middle of the waveguide and the challenges associated with the subsequent substrate removal.

In the case of the III-nitride waveguides, it turns out that a much better variation of the planar polarity inversion is possible. It is based on a peculiar fact that GaN and AlN, naturally grown in the same metal orientation, actually have opposite crystal field orientations and therefore opposite signs of their $\chi^{(2)}$ nonlinear coefficient [26]. In this work, we investigate this novel approach, which is based on composite waveguides containing GaN and AlN layers with intrinsically inverted polarity. Our modelling demonstrates that it is possible to optimize the geometry of these waveguides such that the TM10 second harmonic mode has its lobes separated into layers with opposite signs of the $\chi^{(2)}$ coefficient and at the same time it is phase matched to the TM00 pump mode. Such combination significantly improves the inter-modal overlap and can lead

to high conversion efficiencies, which can reach $30\%\text{W}^{-1}\text{cm}^{-2}$ for a simple ridge waveguide. We validate our modelling results through the first experimental demonstration of an optimized composite GaN/AlN waveguide with an intrinsic polarity inversion. These structures allow us to achieve an experimental conversion efficiency of $4\%\text{W}^{-1}\text{cm}^{-2}$, a value significantly higher than what has been previously reported for simple III-nitride waveguides. The discrepancy between theory and experiment can be explained by the 3.4 dB/cm propagation losses, which were measured for the investigated waveguides.

2. Modelling

In this section, we demonstrate the advantage of the intrinsic planar polarity inversion with the help of a basic $\chi^{(2)}$ nonlinear process: second harmonic generation (SHG). Efficient SHG requires phase matching, which implies that the effective refractive index of the pump must be equal to the one of the second harmonic. To satisfy this condition, the fundamental TM mode must be used for the pump and one of the higher order modes must be used for the second harmonic due to the modal dispersion. However, this choice comes at a cost of a poor modal overlap, as defined by Eq. (1), since the harmonic efficiency is proportional to this overlap factor.

$$\text{overlap} = \left[\iint \chi^{(2)}_{zzz}(x,z) \left(E_z^P(x,z) \right)^2 E_z^{SH}(x,z) \, dx dz \right]^2 \tag{1}$$

For the purpose of demonstration, we have selected a specific configuration involving the TM00 pump mode and the TM10 second harmonic mode. These modes are chosen due to their coupling with the largest nonlinear coefficients for the III-nitrides, represented as $\chi^{(2)}_{zzz}$ (equivalent to $\chi^{(2)}_{33}$). The field profiles of these modes are depicted in Fig. 1(a). Once the modes are determined, the only remaining parameter affecting the overlap integral is the distribution profile of the nonlinear coefficient $\chi^{(2)}$. Interestingly, in the composite waveguides we utilize (as shown in Fig. 1 (a) and (b)), the GaN and AlN layers exhibit opposite signs of $\chi^{(2)}$. Consequently, by appropriately selecting the thickness of the III-nitride layers, we can identify a solution for which the lobes of the TM10 mode are separated between layers having opposite $\chi^{(2)}$ signs. This particular approach significantly enhances the value of the overlap integral.
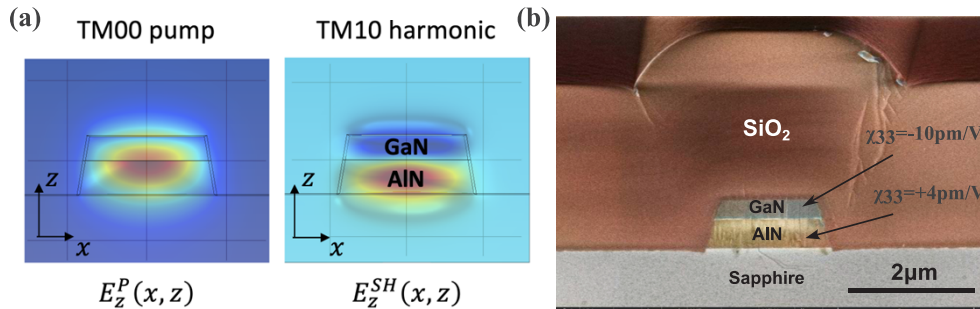

Fig. 1. (a) Distribution of the modes that can be coupled by the $\chi^{(2)}_{zzz}$ coefficient in the second harmonic generation process. The TM00 has one lobe and fills the whole III-nitride waveguide. The TM10 mode has two lobes, one lobe is mainly confined in the GaN layer and the other one in the AlN layer. This configuration allows to reach high values of the overlap integral given by Eq. (1). (b) Facet of the fabricated waveguide showing the two-layer waveguide. GaN and AlN layers have an opposite sign for the nonlinear coefficient $\chi^{(2)}_{zzz}$.

Indeed, in Fig. 2(a) we show the evolution of the predicted SHG efficiency as a function of the AlN thickness in the composite GaN/AlN ridge waveguide with a total III-nitride thickness of

700 nm and a width around 1.5 µm which is slightly adjusted for each given composition in order to satisfy the phase matching conditions. In this calculation, the pump wavelength is set at 1600 nm. We see that the conversion efficiency for pure AlN or GaN waveguides which are most often used is only a fraction of a per cent per Watt per square centimeter. At the same time by choosing the right proportion between GaN and AlN, we can multiply this efficiency by a factor of 100 with the maximum predicted value about $30\%\text{W}^{-1}\text{cm}^{-2}$.
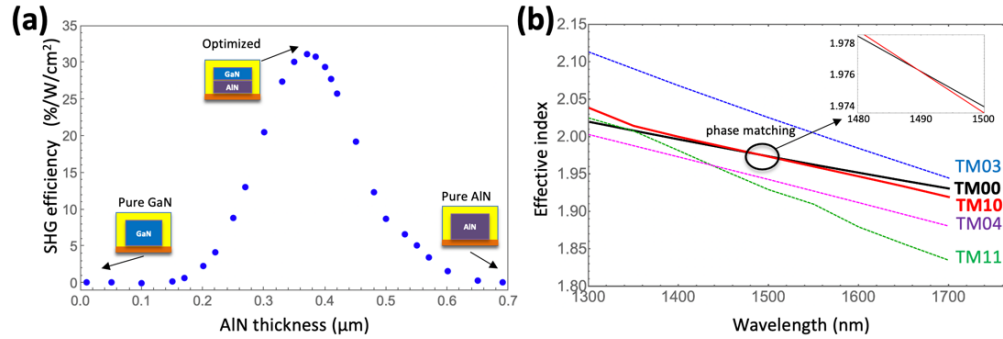

Fig. 2. (a) SHG efficiency as a function of the AlN thickness in composite GaN/AlN waveguides. The total thickness remains constant (700 nm). The width of the waveguide is adjusted for each composition in order to achieve phase matching. There is a clear optimal solution which corresponds to the situation where two lobes of the TM10 modes are separated in GaN and AlN layers. (b) Dispersion curves showing the effective refractive indices of different modes as a function of the wavelength. The dispersion intersection between the TM00 pump and the TM10 harmonic shows a possibility to reach the phase matching conditions in the telecom range for the 700 nm thick and 1.5 µm wide waveguide. The inset in the figure clearly depicts the crossing between the TM00 and TM10 modes.

In the modelling, we did consider the following values for the nonlinear coefficients $\chi^{(2)}_{zzz}(\text{GaN}) = -10\text{pm/V}$, $\chi^{(2)}_{zzz}(\text{AlN}) = +4\text{pm/V}$, as obtained from rotational Maker fringes [26]. The values for the refractive indices were obtained from the references [27] for GaN and [28] for AlN. We note that there is a large dispersion in the absolute values of the second order nonlinear coefficients of GaN and AlN in the literature see e.g. [29]. For AlN, a value of 6 pm/V was deduced from the experimental conversion efficiency in [4] and 8 pm/V in [30]. For GaN, absolute values varying between 16 pm/V [31], 23 pm/V [32] and 10 pm/V [33] were as well reported among others. These values depend on the investigated wavelength (we expect a small wavelength dependence between 1.064 µm and near-infrared), on the type of measurement and on the growth techniques used for the III-nitrides. The sign of the nonlinear coefficients varies as well in the literature and opposite values can be found for the same material. One explanation for this discrepancy is that the sign of the nonlinearity is dependent on the coordinate system used to consider the nonlinear polarization, either the coordinate frame of the crystal or the laboratory reference frame [34]. We note that the enhancement mechanism considered in this work is not dependent on the sign of the nonlinear susceptibility but only relies on the opposite sign between AlN and GaN.

What is even more important is the possibility to reach high overlap values and at the same time preserve modal phase matching. Figure 2(b) shows the dispersion curves for the fundamental TM00 pump mode in black and for the higher order harmonic modes TM10 (red), TM03 (blue), TM11 (green). The intersection between the dispersion curves indicates that the phase matching condition can be achieved. According to our optimization in the telecom spectral range, the maximum overlap and phase matching can be reached in 1.5 µm waveguide width with a 330 nm thick GaN layer on top of a 370 nm thick AlN layer.

There is thus a considerable advantage of the composite GaN/AlN waveguides for a particular enhanced interaction between TM00 pump and TM10 harmonic. It is important to note that there are no other modes configurations between 1400 and 1700 nm that could give comparable efficiencies without polarity inversion.

3. Fabrication

Based on the modelling results, the real structure was fabricated in the following manner. First, a 410 nm thick AlN layer was grown on a sapphire substrate by metalorganic vapor phase epitaxy (MOVPE) at 1150 °C. Then, an additional 290 nm thick GaN layer was grown by molecular beam epitaxy (MBE) at 780°C (Fig. 3(a)). MBE was preferred to MOVPE for the growth of the GaN layer because the GaN surface was smoother. In general, epitaxial growth of III-nitrides is possible on sapphire, Si or SiC substrates. The sapphire was a natural choice for this demonstration because it is transparent in the visible and infrared spectra, and because III-nitrides have a larger refractive index than sapphire, allowing them to naturally form an optically guiding layer. The same process on a SiO_2 substrate is also feasible, but it would require transferring the III-nitride layers from a Si substrate to a SiO_2 substrate. This transfer is achievable, as demonstrated previously in [5] and [31]. However, initially, it would be challenging to grow these specific layers of 410 nm AlN and 290 nm GaN on Si without cracks induced by the strain and the impact of the significant mismatch in thermal expansion coefficients between Si and III-nitrides. To summarize our choice of a sapphire substrate, we can say that it provides a greater flexibility for layer engineering.
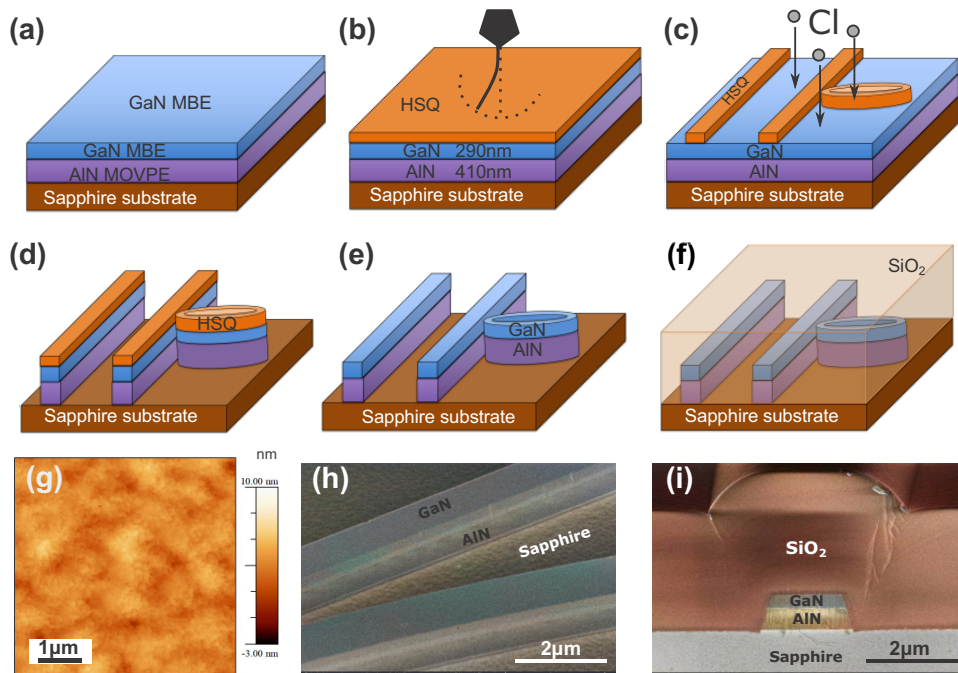

Fig. 3. (a) Initial growth of the AlN layer by MOVPE followed by the growth of the GaN layer by MBE. (b)-(c) HSQ mask preparation by resist spin-coating, electron beam lithography and development. (d)-(e) III-nitride etching by chlorine-based ICP. (f) Encapsulation of the final structure with SiO_2 deposited by PECVD. (g) 5×5 μm^2 atomic force microscopy image of the GaN surface. (h) Scanning electron microscopy (SEM) fragment image of a waveguide coupled to a ring resonator. (i) SEM image of an injection facet.

For a $5 \times 5 \ \mu m^2$ atomic force microscopy (AFM) scan size, the root mean square roughness is below 1 nm for the GaN grown by MBE (Fig. 3(g)) and 10 nm by MOVPE. The GaN grown under our standard GaN MOVPE growth conditions on the 410 nm AlN layers follows an initial three-dimensional growth mode and then a progressive smoothing of the surface. A GaN thickness larger than 500 nm is required to get a fully coalesced GaN layer with these growth conditions. It is probably possible to grow the whole structure by using only the MOVPE reactor after an additional optimization of the GaN growth conditions. The 410 and 290 nm thicknesses for AlN and GaN respectively are close to the values inferred from Fig. 2(a) for a maximum conversion efficiency. We define the etching mask using a negative HSQ e-beam resist and a 80 kV e-beam lithography (Fig. 3(b,c)). The III-nitride layers were etched by chlorine-based inductively-coupled plasma (ICP) and the residues of the HSQ mask were removed by hydrofluoric acid (Fig. 3(d,e)). The etched sidewalls of the waveguides are smooth as it is shown in Fig. 3(h). They are slightly inclined with a 15-degree angle as it is shown in Fig. 3(i). The final structure was encapsulated in a 2 μm thick SiO_2 layer deposited by plasma-enhanced chemical vapor deposition (PECVD) technique (Fig. 3(f) and 3(i) for the real structure).

The fabricated photonic structures include two types of structures. The first type of structure consists of 120 μm diameter ring resonators coupled to 1.5 mm long waveguides which we use for standard transmission experiment in order to estimate the propagation losses. The width of the ring resonators is 1.5 μm. The width of the bus waveguides is 1.3 μm except for the coupling region where it is narrowed down to 0.9 μm. The second type of structure consists of 4.5 mm long waveguides which were designed for the second harmonic experiments. Their width is 1.6 μm. In our opinion, it is convenient to use a basic simple waveguide structure in order to demonstrate the impact of the polarity inversion on the efficiency of the second harmonic generation. Otherwise, it would be difficult to separate the impact of the polarity inversion from other effects like resonance matching in more complicated structures like ring resonators. We chose an end-fire coupling configuration for the light injection into the fabricated photonic structures since the index contrast between III-nitrides and sapphire is not large enough for the realization of an efficient grating coupling. This step is far from trivial in the case of a hard substrate like sapphire. In order to liberate the injection facets, we developed a reproduceable precut and cleaving technique. An example of a cleaved facet is shown in Fig. 3(i).

4. Estimation of the propagation losses

In order to estimate the propagation losses, we use the 120 μm diameter ring resonators coupled to 1.5 mm long waveguides. For light injection, we have used an end-fire coupling without any tapers. Indeed, we employed a cleaving step to release the facets of the waveguides. Sapphire is a challenging substrate to cleave with precision. Consequently, the utilization of tapers was not viable in our situation. We conduct a basic transmission experiment by using a finely tunable laser source in the telecom range. We used a straight-across configuration for the transmission experiment. We both inject and decouple light from the waveguide using Corning fibers with tapered tips at the end. These lensed-fibers have a working distance of 12 μm and a spot size of 2 μm, as compared to the 1 μm^2 cross-section of the waveguide. While tuning the laser and measuring the transmitted signal, we can capture the transmission spectrum, an example of which is shown in Fig. 4. (a)

This spectrum contains periodic oscillations which correspond to the Fabry-Perot resonances defined by the 1.5 mm long waveguide and relatively narrow deeps in the transmission intensity which correspond to the resonances of the 120 μm diameter ring shown in Fig. 4(b). The free spectral range (FSR) of the ring resonances is 2.97 nm for the TM modes and 3.07 nm for the TE modes. We can estimate the group index from the values for the free spectral range. This yields the following values for the TM and the TE modes, respectively: $n_g(TM00) = 2.3$ and
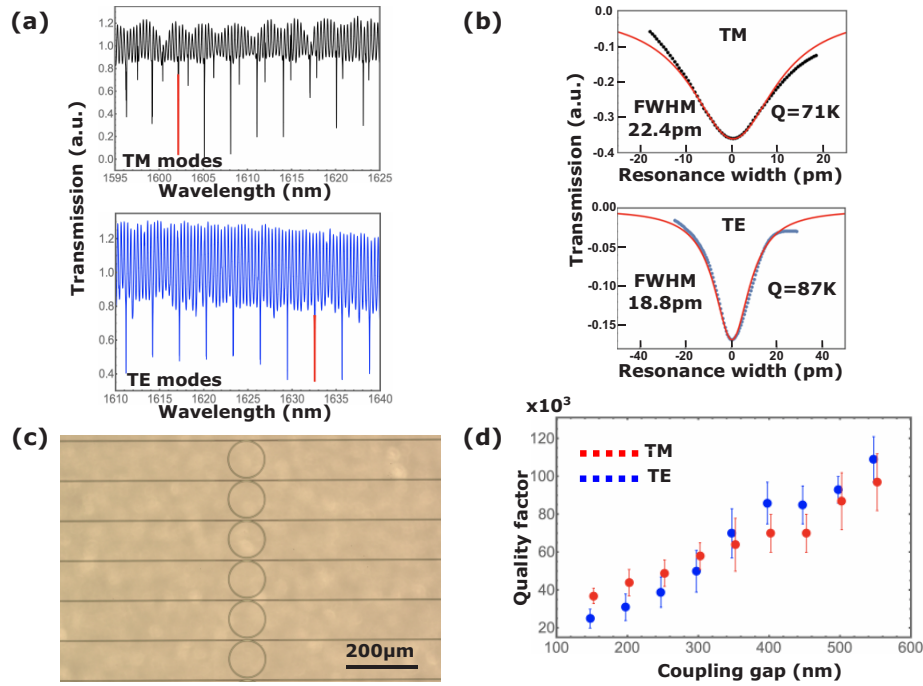
Fig. 4. (a) Typical transmission spectra of a ring resonator for TM and TE modes. (b) Zoom on narrow resonances corresponding to the TM and TE modes in the ring with Lorentzian fit of the data given by the red curves. (c) Microscope image of a group of ring resonators with varying coupling gaps. (d) Loaded quality factors of the ring resonators as a function of the coupling gap between a ring and a waveguide.

n_g(TE00) = 2.27. The width of the rings used for the quality factor measurements is 1.5 μm, which is close to the waveguide width of 1.6 μm used in the second harmonic experiments.

An approximate estimation of the propagation losses can be obtained from the contrast of Fabry-Perot oscillations of the transmitted signal according to the formulas as given by Eq. (2) below [35]:

$$\alpha \, (\text{dB/cm}) = \frac{4.34}{L \, (\text{cm})} \left(lnR - ln \left(\frac{1}{K} \left(1 - \sqrt{1 - K^2} \right) \right) \right), \quad R = \frac{\left(n_{eff} - 1 \right)^2}{\left(n_{eff} + 1 \right)^2}, \qquad K = \frac{I_{max} - I_{min}}{I_{max} + I_{min}} \tag{2}$$

where α corresponds to the propagation losses in dB/cm, L is the length of the waveguide in cm, R is the reflectivity on the facet of the guided mode with a n_{eff} effective refractive index and K is the contrast of the transmitted spectrum defined by the I_{max} and I_{min} – maximum and minimum – transmitted intensities. This estimation gives 3 dB/cm losses for the TM00 mode with n_{eff} = 1.9407 and 2 dB/cm for the TE00 mode with n_{eff} = 1.9565 as calculated for 1.3 μm wide and 1.5 mm long waveguides which we used for the light coupling to the ring resonators. We used R_{TM} = 0.102 and R_{TE} = 0.105 values for the modes reflectivity, which assumes a perfect quality of the facets. Possible variation in the real facet reflectivity introduces an uncertainty in the deduced value of the propagation losses, which is difficult to evaluate, therefore the 3 dB/cm approximate value should be considered only as an estimation.

More precise measurement of the propagation losses can be deduced from the width of the ring resonances. The loaded quality factor of a ring resonator is given by the formula $1/Q_{load} = 1/Q_{coup} + 1/Q_{int}$, where Q_{coup} is the coupling quality factor which is determined by the

coupling between the waveguide and the ring. This coupling depends on the gap distance between the waveguide and the resonator. Q_{int} is the intrinsic quality factor which is determined by the propagation and absorption losses. We fabricated a series of ring resonators with coupling gaps varying from 100 nm up to 550 nm as it is shown in Fig. 4(c) in order to control the coupling and to follow the evolution of the loaded quality factor as a function of the gap distance. It should be noted that the transmission spectra contain significant oscillating parts due to Fabry-Perot resonances, which could have an impact on the accuracy of the quality factor measurement. In order to estimate the error bar in the quality factor value, we performed the Lorentzian fit of the resonances before and after extracting the oscillating part of the spectrum. We observed differences up to 5% in the fitting procedure. If we enforce the strict adjustment of the minima of the Lorentzian fit with the signal during the fitting, the results are more consistent. In contrast, if we leave the amplitude minimum as a free parameter, the fitting results show much more variations, up to an additional 10%. The error bars in Fig. 4(d) include both uncertainties. The is a clear trend: as the coupling decreases, the loaded quality factors tend towards the value of 110 000 for the TE modes and 100 000 for the TM modes. In a highly undercoupled regime, these values are close to the intrinsic quality factors, providing an estimation of the propagation losses of about 3 dB/cm and 3.4 dB/cm for TE and TM modes respectively. The estimations of the losses according to both approaches are very close. Although these losses are higher than the best value of 0.17 dB/cm reported so far, it is still a good result because the waveguides presented in this work are significantly thinner.

The literature on III-nitride waveguides and resonators clearly indicates a trend with thicker and larger waveguides exhibiting in general lower propagation losses. This trend suggests that the sidewall or surface roughness, as well as absorption, are among the primary sources of propagation losses. In our specific case, we have not yet achieved the state-of-the-art quality factors in the million range, despite employing fabrication techniques similar to those used by other groups. Consequently, it might indicate that a significant fraction of the propagation losses originates from material absorption, either in the encapsulating SiO_2 layer or in the nucleation layer at the interface between the III-nitride layers and the sapphire substrate.

5. Second harmonic generation

After the linear characterization of the fabricated photonic structures, we performed a second harmonic generation experiment in the ridge waveguides. The investigated ridge waveguide has a 1.6 µm width. Figure 5(a) shows an example of a SEM image of a ridge waveguide before the SiO_2 encapsulation revealing the smooth nature of the waveguide sidewalls after the etching. We inject the telecom tunable pump as before using an end-fire coupling scheme with a lensed fiber. The fiber allows to control the polarization of the light, so we chose to inject into a TM mode in order to use the TM → TM conversion associated with the largest nonlinear coefficient $\chi^{(2)}_{zzz}$. We estimate the injection losses for the pump to be around 5 dB. In the present experiment, the laser can be continuously tuned from 1560 nm to 1685 nm. We chose the width of the waveguide so that the phase matching can be found in this spectral window. Indeed, while tuning the wavelength of the laser at 13 dBm power, we observe some faint second harmonic signal with a sensitive CMOS camera which corresponds to the harmonic conversion without phase matching.

As soon as we approach the phase matching wavelength which is around 1675 nm, the signal increases rapidly and can be easily measured with a standard Si detector. We used a Newport 818-SL detector for measuring the second harmonic power around 840 nm. This detector has a minimum measurable power of 20 pW and exhibits approximately 1 pW of dark noise. The detector is not sensible to the wavelengths in the near-infrared spectrum, specifically at the 1680 nm wavelength of the pump. In proximity to the phase matching wavelength, the incident harmonic power measured by the detector is approximately 10 nW. This signal clearly corresponds to the second harmonic one, rather than a parasitic signal from the pump, for two
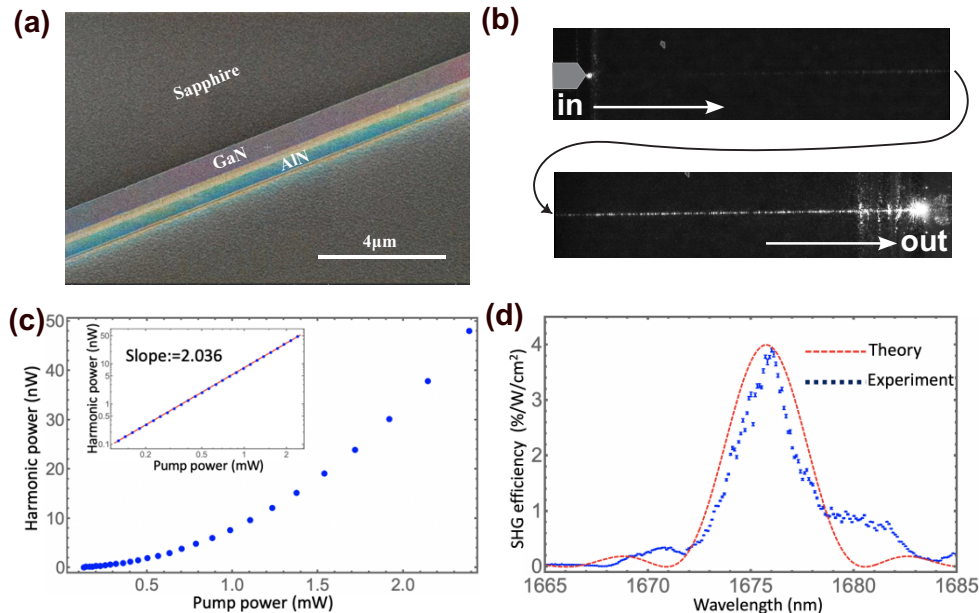
Fig. 5. (a) SEM image of the waveguide used for the SHG experiment. (b) Images of the second harmonic generation in the 4.5 mm long waveguide. Since the waveguide is long, only entrance (top) and exit (bottom) parts are shown. (c) Power of the second harmonic as a function of the injected pump power. Linear fit of the log plot shows a quadratic dependence corresponding to the second harmonic generation. (d) Normalized second harmonic efficiency as the function of the pump wavelength.

distinct reasons. The first reason is attributed to the narrow resonant signature of the signal, diminishing from 10 nW to few hundreds of pW within a 20 nm range from its peak. Upon extending our observation beyond this resonance region, the signal declines further, dropping below 20 pW and even beneath 1 pW around 1560 nm. This phenomenon occurs despite the pump continuing to deliver a consistent power in the waveguide. The second reason stems from the observation of the scattered harmonic light using a Si camera, as shown in Fig. 5(b). We clearly observe that the intensity of the signal increases along the waveguide when we reach the phase matching conditions. This would not be the case if it was merely light scattered from the 1680 nm pump.

At the signal maximum, we deduce a power of 50 nW of continuous second harmonic generated inside the waveguide from the 2.4 mW of the guided pump power as shown in Fig. 5(c). This corresponds to a $4\%\mathrm{W}^{-1}\mathrm{cm}^{-2}$ conversion efficiency which is a very good result for a simple waveguide. Figure 5(d) shows the so-called phase matching curve which gives the efficiency of the second harmonic generation as a function of the pump wavelength. At the 1675 nm wavelength which corresponds to the maximum, we measure the second harmonic signal as a function of the injected pump power. Figure 5(c) shows this dependence both in linear and log plots and shows the quadratic dependence of the harmonic power as a function of the pump power which further confirms that this is indeed a second harmonic generation process. At each point presented in Fig. 5, both the second harmonic and the pump signals were averaged over 10 sec by using 10 000 samples of 1ms acquisitions. The points on the graphs represent the average values. The deviations from the average remain small. They are barely noticeable in Fig. 5(d) as error bars on the blue curve. The measurements under the same conditions would not yield any signal on the 818-SL detector far from the phase matching conditions.

The width of the acceptance curve is determined by the length of the waveguide and by the relative dispersion of the interacting modes. In the ideal waveguide, the shape of the curve is determined by the squared sinus cardinal function following Eq. (3):

$$\eta = \eta_0 sinc^2 \{\Delta\beta L/2\} = \eta_0 sinc^2 \left\{ \left(\beta_{sh} - 2\beta_p\right) L/2 \right\} = \eta_0 sinc^2 \left\{ \frac{2\pi}{\lambda} \left(n_{sh}\left(\lambda/2\right) - n_p\left(\lambda\right)\right) L \right\} \quad (3)$$

where L is the length of the waveguide, λ is the wavelength of the pump, n_{sh}, n_p are effective refractive indices of the second harmonic and the pump respectively. η_0 corresponds to the SHG conversion efficiency when the phase matching conditions are perfectly satisfied. In the Eq. (3), η_0 is used as a fitting parameter for the experimental data presented in Fig. 5(d). Using this model and the dispersion curves for the TM00 and TM10 interacting modes from the Fig. 2(b), we can predict the theoretical acceptance curve which is shown by the red dashed line in Fig. 5(d).

In the previous section, we did estimate the propagation losses to be around 3.4 dB/cm in the infrared. According to measurements reported in [36], we can expect the propagation losses in the visible to be as high as 16 dB/cm. Using these values for the propagation losses, we can estimate the expected efficiency drop from the perfect value of $30\%W^{-1}cm^{-2}$ (η) by the formula given in Eq. (4):

$$\eta_{loss} = \eta exp\left[-\left(\alpha_\omega + \alpha_{2\omega}/2\right)L\right] \frac{sinh^2\left[\left(\alpha_\omega - \alpha_{2\omega}/2\right)L/2\right]}{\left(\alpha_\omega - \alpha_{2\omega}/2\right)L/2^2} \quad (4)$$

where L is the length of the waveguide in cm and α_ω, $\alpha_{2\omega}$ are the propagation losses for the pump and the second harmonic given in the cm^{-1} units. This estimation gives $9\%W^{-1}cm^{-2}$ theoretical conversion in a waveguide with losses, which is close to the measured experimental value of $4\%W^{-1}cm^{-2}$. It appears that the minimization of the optical losses in the visible represents an important milestone to further improve the experimental conversion efficiency.

6. Discussion

In this work, we report the first successful demonstration of III-nitride waveguides with an intrinsic polarity inversion obtained directly from the epitaxial growth. The performance of previously reported structures either with the planar polarity inversion [37] or with the periodic polarity inversion [38] was significantly reduced by the high propagation losses associated with the complexity of the fabrication process. Consequently, the conversion efficiencies remained low both for planar ($5.2 \times 10^{-3}\%W^{-1}cm^{-2}$) and periodic structures ($1.5 \times 10^{-4}\%W^{-1}cm^{-2}$). The present fabrication approach is simple since it does not require bonding of layers with an opposite polarity or the periodic pattering and regrowth. As a result, we observe moderate propagation losses along with a conversion efficiency which is already higher than the values that was obtained in the simple GaN waveguides ($0.15\%W^{-1}cm^{-2}$) [39], Si_3N_4-on-insulator waveguides ($0.05\%W^{-1}cm^{-2}$) [40] and GaP-on-insulator waveguides ($0.4\%W^{-1}cm^{-2}$) [41]. This value is still behind the values reported for waveguides with a high confinement and high nonlinear coefficients such as oxidized AlGaAs waveguides ($1120\%W^{-1}cm^{-2}$) [42], thin film lithium niobate (TFLN) waveguides ($41\%W^{-1}cm^{-2}$) [43], GaAs on insulator (GaAsOI) ($47000\%W^{-1}cm^{-2}$) [44] and low loss structures with the periodic polarity inversion such as orientation-patterned OP-AlGaAs ($46\%W^{-1}cm^{-2}$) [45], OP-GaP ($200\%W^{-1}cm^{-2}$) [46], buried periodically poled lithium niobate (PPLN) ($150\%W^{-1}cm^{-2}$) [47] or PPLN-on-insulator ($3757\%W^{-1}cm^{-2}$) [48]. It is not surprising that those materials provide much better conversion efficiencies since they have much larger second order nonlinear coefficients with typical values reported in the literature: $d_{33}(LN) = 27$ pm/V, $d_{14}(GaP) = 50$ pm/V, $d_{14}(GaAs) = 110$ pm/V in comparison to $d_{33}(GaN) = 5$ pm/V. Periodic polarity inversion with low propagation losses clearly demonstrates the interest of the nonlinear interactions between the fundamental modes. There is still an interest though in studying

III-nitrides in spite of their relatively low nonlinear coefficient because their wide band gap provides a significantly larger transparency window spanning from the UV to the mid-IR and allows to avoid the problems of the two-photon absorption and photo-refraction which are associated with the materials mentioned above.

The results reported above are obtained in a simple ridge waveguide and there is still another round of improvement to make by applying the same principles in the III-nitride resonators. Indeed, the initial conversion efficiency of a fraction of a percent for III-nitride waveguides was progressively transformed into rather impressive values of $2500\%W^{-1}$ [49] and finally $17000\%W^{-1}$ [4] by developing high quality ring resonators reaching Q = 1 Million and optimizing the phase matching by geometry and temperature tuning. The same approach allowed to go even further in InGaP ring resonators up to $71000\%W^{-1}$ [50] and PPLN with $5\%\mu W^{-1}$ with Q = 2 Million ring resonators [51].

The polarity inversion in our structures is obtained naturally by a standard growth technique so there is no reason why we could not reach the reported quality factors along with an additional optimization of growth and fabrication. This would open new interesting opportunities for nonlinear interactions with even higher efficiencies in III-nitrides with polarity inversion. It should be noted that this property of the III-nitrides is rather unique as it allows a relatively easy improvement of the conversion efficiency by two orders of magnitude in comparison to the simple GaN or AlN waveguides. Our approach could naturally be used not only for classical but also for quantum sources. By proper adjustment of the GaN/AlN configuration, it could provide an efficient photon pair source based on the spontaneous down-conversion in the whole transparency window of III-nitrides and the advantage to reach the telecom wavelength with a pump in the visible.

7. Conclusions

We investigated a novel approach for nonlinear interactions based on composite GaN/AlN waveguides. Although both of the III-nitride layers are grown in the same metal orientation, it turns out that they exhibit opposite signs of the $\chi^{(2)}$ nonlinear coefficient. This peculiar and unique property offers an opportunity to address the issue of modal overlap and enhance the conversion efficiency by two orders of magnitude as compared to simple GaN or AlN waveguides. Theoretical investigations indicate that an efficiency of $30\%W^{-1}cm^{-2}$ can be achieved. We confirmed this theoretical estimation through an experimental demonstration, obtaining a conversion efficiency of $4\%W^{-1}cm^{-2}$. Further improvements are expected by reducing the propagation losses. The use of ring resonators with high quality factors should provide an alternative approach to demonstrate very high conversion efficiencies for second order nonlinear processes.

Disclosures. The authors declare no conflict of interest.

Data availability. Data underlying the results presented in this paper are not publicly available at this time but may be obtained from the authors upon reasonable request

References
1. D. J. Blumenthal, "Photonic integration for UV to IR applications," APL Photonics **5**(2), 20903 (2020).
2. S. Bogdanov, M. Y. Shalaginov, A. Boltasseva, and V. M. Shalaev, "Material platforms for integrated quantum photonics," Opt. Mater. Express **7**(1), 111 (2017).
3. C. A. Husko, A. S. Clark, M. J. Collins, A. De Rossi, S. Combrié, G. Lehoucq, I. H. Rey, T. F. Krauss, C. Xiong, and B. J. Eggleton, "Multi-photon absorption limits to heralded single photon sources," Sci. Rep. **3**(1), 3087 (2013).

4. A. W. Bruch, X. Liu, X. Guo, J. B. Surya, Z. Gong, L. Zhang, J. Wang, J. Yan, and H. X. Tang, "17 000%/W second-harmonic conversion efficiency in single-crystalline aluminum nitride microresonators," Appl. Phys. Lett. **113**(13), 131102 (2018).

5. M. Gromovyi, M. El Kurdi, X. Checoury, E. Herth, F. Tabataba-Vakili, N. Bhat, A. Courville, F. Semond, and P. Boucaud, "Low-loss GaN-on-insulator platform for integrated photonics," Opt. Express **30**(12), 20737 (2022).

6. M. S. Mohamed, A. Simbula, J. F. Carlin, M. Minkov, D. Gerace, V. Savona, N. Grandjean, M. Galli, and R. Houdré, "Efficient continuous-wave nonlinear frequency conversion in high-Q gallium nitride photonic crystal cavities on silicon," APL Photonics **2**(3), 31301 (2017).

7. Y. Zeng, I. Roland, X. Checoury, Z. Han, M. El Kurdi, S. Sauvage, B. Gayral, C. Brimont, T. Guillet, M. Mexis, F. Semond, and P. Boucaud, "Resonant second harmonic generation in a gallium nitride two-dimensional photonic crystal on silicon," Appl. Phys. Lett. **106**(8), 81105 (2015).

8. H. X. Tang, C.-L. Zou, A. W. Bruch, X. Liu, and J. B. Surya, "On-chip $\chi^{(2)}$ microring optical parametric oscillator," Optica **6**(10), 1361–1366 (2019).

9. Y. Zheng, C. Sun, B. Xiong, L. Wang, Z. Hao, J. Wang, Y. Han, H. Li, J. Yu, and Y. Luo, "Integrated Gallium Nitride Nonlinear Photonics," Laser Photon. Rev. **16**(1), 2100071 (2022).

10. X. Liu, Z. Gong, A. W. Bruch, J. B. Surya, J. Lu, and H. X. Tang, "Aluminum nitride nanophotonics for beyond-octave soliton microcomb generation and self-referencing," Nat. Commun. **12**(1), 5428 (2021).

11. K. Mizuuchi, K. Yamamoto, T. Sugita, and Y. Kitaoka, "31%-efficient blue second-harmonic generation in a periodically poled MgO:LiNbO$_3$ waveguide by frequency doubling of an AlGaAs laser diode," Opt. Lett. **24**(22), 1590–1592 (1999).

12. M. V. O'Connor, C. B. E. Gawith, P. G. R. Smith, K. Gallo, L. Ming, and G. D. Emmerson, "High conversion efficiency single-pass second harmonic generation in a zinc-diffused periodically poled lithium niobate waveguide," Opt. Express **13**(13), 4862–4868 (2005).

13. M. M. Fejer and J.-P. Meyn, "Tunable ultraviolet radiation by second-harmonic generation in periodically poled lithium tantalate," Opt. Lett. **22**(16), 1214–1216 (1997).

14. N. E. Yu, S. Kurimura, Y. Nomura, M. Nakamura, K. Kitamura, J. Sakuma, Y. Otani, and A. Shiratori, "Periodically poled near-stoichiometric lithium tantalate for optical parametric oscillation," Appl. Phys. Lett. **84**(10), 1662–1664 (2004).

15. F. Torabi-Goudarzi and E. Riis, "Efficient cw high-power frequency doubling in periodically poled KTP," Opt. Commun. **227**(4-6), 389–403 (2003).

16. M. Fiorentino, S. M. Spillane, R. G. Beausoleil, T. D. Roberts, P. Battle, M. W. Munro, P. G. Kwiat, K. Mattle, H. Weinfurter, A. Zeilinger, D. Riedmatten, H. Tittel, H. Zbinden, P. Baldi, M. De Micheli, D. B. Ostrowsky, and N. Gisin, "Spontaneous parametric down-conversion in periodically poled KTP waveguides and bulk crystals," Opt. Express **15**(12), 7479–7488 (2007).

17. S. Pezzagna, P. Vennéguès, N. Grandjean, A. D. Wieck, and J. Massies, "Submicron periodic poling and chemical patterning of GaN," Appl. Phys. Lett. **87**(6), 062106 (2005).

18. J. Hite, M. Twigg, M. Mastro, J. Freitas, J. Meyer, I. Vurgaftman, S. O'Connor, N. Condon, F. Kub, S. Bowman, and C. Eddy, "Development of periodically oriented gallium nitride for non-linear optics," Opt. Mater. Express **2**(9), 1203–1208 (2012).

19. D. Alden, W. Guo, R. Kirste, F. Kaess, I. Bryan, T. Troha, A. Bagal, P. Reddy, L. H. Hernandez-Balderrama, A. Franke, S. Mita, C. H. Chang, A. Hoffmann, M. Zgonik, R. Collazo, and Z. Sitar, "Fabrication and structural properties of AlN submicron periodic lateral polar structures and waveguides for UV-C applications," Appl. Phys. Lett. **108**(26), 261106 (2016).

20. D. Alden, T. Troha, R. Kirste, S. Mita, Q. Guo, A. Hoffmann, M. Zgonik, R. Collazo, and Z. Sitar, "Quasi-phase-matched second harmonic generation of UV light using AlN waveguides," Appl. Phys. Lett. **114**(10), 103504 (2019).

21. A. Fiore, V. Berger, E. Rosencher, P. Bravetti, and J. Nagle, "Phase matching using an isotropic nonlinear optical material," Nature **391**(6666), 463–466 (1998).

22. J. M. Dallesasse, N. Holonyak, A. R. Sugg, T. A. Richard, and N. El-Zein, "Hydrolyzation oxidation of Al$_x$Ga$_{1-x}$As-AlAs-GaAs quantum well heterostructures and superlattices," Appl. Phys. Lett. **57**(26), 2844–2846 (1990).

23. E. Guillotel, M. Ravaro, F. Ghiglieno, C. Langlois, C. Ricolleau, S. Ducci, I. Favero, and G. Leo, "Parametric amplification in GaAs/AlOx waveguide," Appl. Phys. Lett. **94**(17), 171110 (2009).

24. S. Pezzagna, P. Vennéguès, N. Grandjean, and J. Massies, "Polarity inversion of GaN(0001) by a high Mg doping," J. Cryst. Growth **269**(2-4), 249–256 (2004).

25. N. Yokoyama, R. Tanabe, Y. Yasuda, H. Honda, S. Ichikawa, Y. Fujiwara, T. Hikosaka, M. Uemukai, T. Tanikawa, and R. Katayama, "GaN channel waveguide with vertically polarity inversion formed by surface activated bonding for wavelength conversion," Jpn. J. Appl. Phys. **61**(5), 050902 (2022).

26. N. A. Sanford, A. V. Davydov, D. V. Tsvetkov, A. V. Dmitriev, S. Keller, U. K. Mishra, S. P. Denbaars, S. S. Park, J. Y. Han, and R. J. Molnar, "Measurement of second order susceptibilities of GaN and AlGaN," J. Appl. Phys. **97**(5), 053512 (2005).

27. S. Pezzagna, J. Brault, M. Leroux, J. Massies, and M. De Micheli, "Refractive indices and elasto-optic coefficients of GaN studied by optical waveguiding," J. Appl. Phys. **103**(12), 1–8 (2008).

28. Ü. Özgür, G. Webb-Wood, H. O. Everitt, F. Yun, and H. Morkoç, "Systematic measurement of $Al_xGa_{1-x}N$ refractive indices," Appl. Phys. Lett. **79**(25), 4103–4105 (2001).

29. N. Vermeulen, D. Espinosa, and A. Ball, *et al.*, "Post-2000 nonlinear optical materials and measurements: Data tables and best practices," J. Phys. Photonics **5**(3), 035001 (2023).

30. A. Majkić, A. Franke, R. Kirste, R. Schlesser, R. Collazo, Z. Sitar, and M. Zgonik, "Optical nonlinear and electro-optical coefficients in bulk aluminium nitride single crystals," Phys. Status Solidi B **254**(9), 1700077 (2017).

31. C. Xiong, W. Pernice, K. K. Ryu, C. Schuck, K. Y. Fong, T. Palacios, H. X. Tang, J. U. Fürst, D. V Strekalov, D. Elser, M. Lassen, U. L. Andersen, C. Marquardt, and G. Leuchs, "Integrated GaN photonic circuits on silicon (100) for second harmonic generation," Opt. Express **19**(11), 10462–10470 (2011).

32. I. V. Kravetsky, I. M. Tiginyanu, R. Hildebrandt, G. Marowsky, A. Pavlidis, A. Eisenbach, and H. L. Hartnagel, "Nonlinear optical response of GaN layers on sapphire: The impact of fundamental beam interference," Appl. Phys. Lett. **76**(7), 810–812 (2000).

33. M. C. Larciprete, M. Centini, A. Belardini, L. Sciscione, M. Bertolotti, C. Sibilia, M. Scalora, A. Passaseo, and B. Poti, "Second harmonic generation in $GaN/Al_{50}Ga_{50}N$ films deposited by metal-organic chemical vapor deposition," Appl. Phys. Lett. **89**(13), 131105 (2006).

34. J. Miragliotta, D. K. Wickenden, T. J. Kistenmacher, and W. A. Bryden, "Linear- and nonlinear-optical properties of GaN thin films," J. Opt. Soc. Am. B **10**(8), 1447 (1993).

35. R. Regener and W. Sohler, "Loss in low-finesse Ti:LiNbO3 optical waveguide resonators," Appl. Phys. B **36**(3), 143–147 (1985).

36. A. Stolz, E. Cho, E. Dogheche, Y. Androussi, D. Troadec, D. Pavlidis, and D. Decoster, "Optical waveguide loss minimized into gallium nitride based structures grown by metal organic vapor phase epitaxy," Appl. Phys. Lett. **98**(16), 161903 (2011).

37. N. Yokoyama, Y. Morioka, T. Murata, H. Honda, K. Serita, H. Murakami, M. Tonouchi, S. Tokita, S. Ichikawa, Y. Fujiwara, T. Hikosaka, M. Uemukai, T. Tanikawa, and R. Katayama, "Second harmonic generation in GaN transverse quasi-phase-matched waveguide pumped with femtosecond laser," Appl. Phys. Express **15**(11), 112002 (2022).

38. H. Ishihara, K. Shimada, S. Umeda, N. Yokoyama, H. Honda, K. Kurose, K. Kawata, A. Sugita, Y. Inoue, M. Uemukai, T. Tanikawa, R. Katayama, and T. Nakano, "Fabrication and evaluation of rib-waveguide-type wavelength conversion devices using GaN-QPM crystals," Jpn. J. Appl. Phys. **61**(SK), SK1020 (2022).

39. M. Gromovyi, J. Brault, A. Courville, S. Rennesson, F. Semond, G. Feuillet, P. Baldi, P. Boucaud, J.-Y. Duboz, and M. P. De Micheli, "Efficient second harmonic generation in low-loss planar GaN waveguides," Opt. Express **25**(19), 23035–23044 (2017).

40. A. Billat, D. Grassani, M. H. P. Pfeiffer, S. Kharitonov, T. J. Kippenberg, and C. S. Brès, "Large second harmonic generation enhancement in Si3N4 waveguides by all-optically induced quasi-phase-matching," Nat. Commun. **8**(1), 1016 (2017).

41. A. P. Anthur, H. Zhang, Y. Akimov, J. R. Ong, D. Kalashnikov, A. I. Kuznetsov, and L. Krivitsky, "Second harmonic generation in gallium phosphide nano-waveguides," Opt. Express **29**(7), 10307–10320 (2021).

42. A. Lemaître, M. Savanier, G. Leo, C. Manquest, E. Galopin, A. Andronico, I. Favero, and S. Ducci, "Large second-harmonic generation at 1.55 μm in oxidized AlGaAs waveguides," Opt. Lett. **36**(15), 2955–2957 (2011).

43. G.-C. Guo, C. Wang, X. Xiong, X.-F. Ren, M. Lončar, N. Andrade, and V. Venkataraman, "Second harmonic generation in nano-structured thin-film lithium niobate waveguides," Opt. Express **25**(6), 6963–6973 (2017).

44. E. J. Stanton, J. Chiles, N. Nader, G. Moody, G. Moody, N. Volet, L. Chang, J. E. Bowers, S. W. Nam, and R. P. Mirin, "Efficient second harmonic generation in nanophotonic GaAs-on-insulator waveguides," Opt. Express **28**(7), 9521–9532 (2020).

45. X. Yu, L. Scaccabarozzi, J. S. Harris, P. S. Kuo, and M. M. Fejer, "Efficient continuous wave second harmonic generation pumped at 1.55 μm in quasi-phase-matched AlGaAs waveguides," Opt. Express **13**(26), 10742–10748 (2005).

46. K. Pantzas, S. Combrié, M. Bailly, R. Mandouze, F. R. Talenti, A. Harouri, B. Gerard, G. Beaudoin, L. Le Gratiet, G. Patriarche, A. De Rossi, Y. Leger, I. Sagnes, and A. Grisard, "Continuous-Wave Second-Harmonic Generation in Orientation-Patterned Gallium Phosphide Waveguides at Telecom Wavelengths," ACS Photonics **9**(6), 2032–2039 (2022).

47. R. V. Roussev, M. M. Fejer, M. Fujimura, K. R. Parameswaran, J. R. Kurz, and R. K. Route, "Highly efficient second-harmonic generation in buried waveguides formed by annealed and reverse proton exchange in periodically poled lithium niobate," Opt. Lett. **27**(3), 179–181 (2002).

48. J. Zhao, M. Rüsing, U. A. Javid, J. Ling, M. Li, Q. Lin, Q. Lin, and S. Mookherjea, "Shallow-etched thin-film lithium niobate waveguides for highly-efficient second-harmonic generation," Opt. Express **28**(13), 19669–19682 (2020).

49. X. Guo, C. Zou, and H. Tang, "Second-harmonic generation in aluminum nitride microrings with 2500%/W conversion efficiency," Optica **3**(10), 1126 (2016).

50. M. Zhao and K. Fang, "InGaP quantum nanophotonic integrated circuits with 1.5% nonlinearity-to-loss ratio," Optica **9**(2), 258–263 (2022).

51. H. X. Tang, C.-L. Zou, M. Li, J. Lu, and A. Al Sayem, "Toward 1% single-photon anharmonicity with periodically poled lithium niobate microring resonators," Optica **7**(12), 1654–1659 (2020).